Progress In Electromagnetics Research, Vol. 145, 1–10, 2014

GPR Signal Enhancement Using Sliding-Window Space-Frequency Matrices

Mehmet E. Yavuz[1, *], Ahmed E. Fouda[2], and Fernando L. Teixeira[3]

Abstract—Ground penetrating radar (GPR) has shown to provide useful results for detection of buried objects. However, its performance suffers from strong reflection from ground surface especially for shallowly buried targets. In such cases, the detection problem depends on the separation of the target signal from the ground backscatter such as landmines and unexploded ordnances. In this paper, we discuss and analyze the use of space-frequency time-reversal matrices for the enhancement of ground penetrating radar signals and potential clutter reduction. Through the use of sliding windows, submatrices from a given B-scan (radargram) are utilized to extract localized scattering information of a given detection scenario. Each sub-B-scan is decomposed to its singular vectors and later used to render synthetic aperture time-domain singular vector distributions corresponding to different scattering mechanisms. Later, they are weighted by the singular values and subtracted from the full B-scan to achieve reduced clutter and enhanced target response. The method shows satisfactory results for shallowly buried dielectric targets even in the presence of rough surface profiles.

1. INTRODUCTION

Ground-penetrating radar (GPR) is a well-established (geophysical) remote sensing method used to obtain information on the subsurface [1]. It is extensively utilized in various fields such as shallow geophysical exploration, civil engineering and archeology [1]. Thanks to its strong detection potential, it is one of the preferred methods in detection and localization of buried objects such as land mines, unexploded ordnances or utilities. GPR exploits the differences between the electromagnetic characteristics, such as the dielectric permittivity and the conductivity of a surrounding medium and the target of interest to achieve detection. In many applications, GPR data is often hampered by clutter which is mainly composed of (rough) surface reflection, scattering from third party objects and cross-talk between antennas. Also, particularly for shallow buried objects, temporal responses of the surface and the targets can overlap and interfere each other thereby eliminating the option of time-gating for improved GPR responses. Additionally, in case of lossy subsurface and dielectric targets (e.g., plastic mines), scattered energy from the targets can be very low. Thus, GPR performance highly depends on the ability to successfully differentiate the target signal from the clutter. One of the main topic of interest in GPR signal processing is therefore geared towards the reduction of clutter. Various studies have been conducted on this front, among them are filtering algorithms [2–4], parametric system identification [5], statistical signal processing [6], subspace methods [7–9], entropy-based approaches [10] and techniques employing parametric and non-parametric modeling [11]. A neural networks approach has been introduced in the marine radar application [12] for sea clutter reduction and other approaches have been successfully used in automatic radar detection in ground clutter [13, 14]. While each method tackles different aspects of the problem, there is still room for further improvement.

Received 1 January 2014, Accepted 7 February 2014, Scheduled 11 February 2014

[*] Corresponding author: Mehmet Emre Yavuz (yavuz.5@osu.edu).

[1] Intel Corporation, Portland, OR, United States. [2] Halliburton Energy Services, Houston, TX, United States. [3] Ohio State University, Columbus, OH, United States.

In this study, we present a singular value decomposition (SVD) based method for improved detection of shallow dielectric targets (e.g., plastic landmines). The method was first applied in a time-reversal (TR) based imaging algorithm utilizing space-frequency (SF) matrices [15]. TR has been first introduced in acoustics [16] and attracted attention from different disciplines such as communications [17] and electromagnetics [18]. Two recent studies have already applied TR in the GPR field [19, 20]. TR can achieve both temporal and spatial focusing around the original target location(s) thanks to the exploitation of wave equation reciprocity in lossless and time-invariant media. Its ability to positively exploit the multipaths in the medium yields to superresolution and statistical stability [16]. Here, we adapt the SF-TR matrices proposed in [15] for its potential application to GPR detection of shallowly buried dielectric targets. As discussed in [4, 21] and elsewhere, target signature in such cases is hidden in a strong clutter signal, thus poses an important challenge. In our attempt to extract the target signature in the presence of strong clutter, we develop a method based on spatially sliding windows and synthesizing singular vector distributions corresponding to different scattering mechanisms. We apply the SVD to the appropriately selected subsets of radargrams (B-scan) obtained during a given GPR survey. A radargram is obtained by the collection of individual A-scans each of which corresponds to the recorded GPR response at a single location. Basically, when the GPR is away from the target of interest, the radargram mainly carries the (rough) surface information and when the GPR is in the vicinity of the target of interest, the radargram contains both surface and target responses. When the SVD is applied to different subsections of the radargram, the singular values and corresponding vectors can be combined to synthesize time-domain signals that correspond to different scattering centers. They can later be subtracted from the full B-scan for reduction of surface clutter and enhancement of target response. In the next sections, we introduce the method and support it with various sample scenarios.

2. SYNTHETIC APERTURE SPACE-FREQUENCY DATA MATRIX GENERATION AND UTILIZATION

We consider a pulse radar GPR system with a *single* transmitter-receiver to illustrate the method (Fig. 1). An extension to array configuration is possible and left for future works due to space limitation. For better articulation, alongside with the fundamentals of the method, we provide results obtained from numerical simulations based on the finite-difference time-domain method [22]. The utilized GPR antenna located 10 cm above the ground surface transmits a short pulse of 900 MHz and the scattered signals are recorded back at the same location. Since the antenna has a low directivity, a single measurement is not enough to decide on the target direction. Thus, it is assumed that the GPR unit moves along the $+x$-direction while surveying. At a given spatial location ($\vec{r}_i$) above the ground, the time domain response recorded by the GPR unit is called an A-scan and denoted by $A(\vec{r}_i, t)$. Each A-scan signal can be modeled as a summation of three independent parts, $A(\vec{r}_i, t) = s_i(t) + b_i(t) + n_i(t)$ where $s_i(t)$ is the desired target signal, $b_i(t)$ is the background return and $n_i(t)$ is the remaining clutter and noise. An ensemble of A-scans obtained at various spatial locations forms the so-called B-scan (radargram) which is represented by

$$\mathbf{B}\left(\mathbf{R}_1^N, t\right) = [A(\vec{r}_1, t), \ldots, A(\vec{r}_N, t)] \tag{1}$$

where N is the total number of A-scans and $\mathbf{R}_i^j = [\vec{r}_i, \ldots, \vec{r}_j]$ with $j \geq i$. B-scans obtained for a dielectric target of 5 cm radius and $\epsilon_r = 3$ embedded 5 cm below the uniform and randomly fluctuating surface profiles of $\epsilon_r = 9$ (dry clay) are shown in Fig. 1. The rough surface generation follows random medium generation of [22]. These chosen parameters, i.e., relative dielectric permittivity and the depth information are similar to those provided in [5, 21]. As the target is shallowly buried and the target-soil dielectric contrast is smaller compared to air-subsurface contrast, this constitutes a difficult detection problem with a low signal to noise ratio. Note also that the algorithm can also be applied to lossy media without loss of generality.

If the individual A-scans forming the B-scan are Fourier transformed in time, the frequency domain B-scan $\mathbf{B}(\mathbf{R}_1^N, \omega)$ is obtained which is essentially similar in form to the space-frequency (SF) TR matrix of [15]. However, while the SF matrix of [15] utilizes an array of $N > 1$ static antennas, $\mathbf{B}(\mathbf{R}_1^N, \omega)$ is obtained using a single transceiver at different survey locations mimicking synthetic aperture behavior. Owing to this similarity, space-frequency TR algorithm can in principle be applied to the full B-scan.

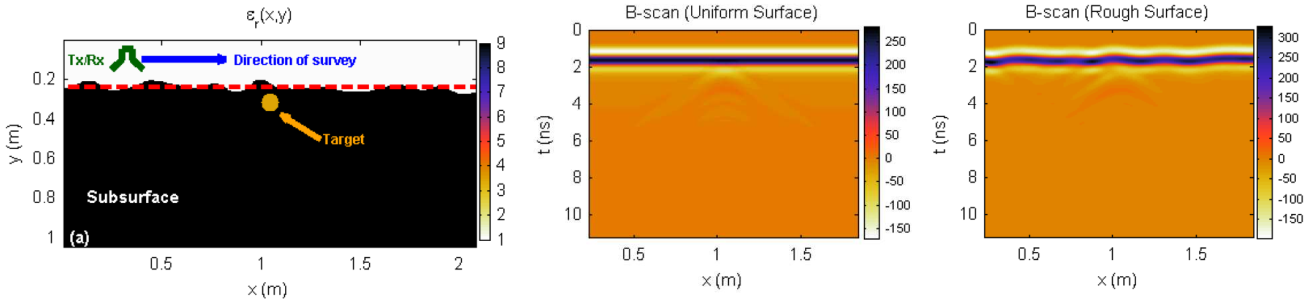

(a) (b) (c)

Figure 1. (a) A GPR surveying scenario where a dielectric target of $\epsilon_r = 3$ is embedded below a rough surface profile with $\epsilon_r = 9$ (dry clay). The dashed line represents the corresponding uniform surface interface. (b) Full B-scan obtained with uniform and (c) rough surface.

In the SF-TR algorithm, SVD is applied to the chosen data matrix to obtain the coherent time-domain singular vectors that can be later used for backpropagation [15] or extracting target signatures [23]. In the GPR problem, if the spatial range of the B-scan is relatively large such that the individual A-scans have both target and surface signatures with different direction of arrivals, delays and amplitudes, then the obtained time-domain singular vectors do not necessarily represent the scattering centers accurately. However, with a shorter spatial range, it might be possible to extract the signatures due to different scattering components more effectively. Hence, in an effort to adapt the technique for its successful application to the GPR scenario, several modifications are introduced. First, instead of using the global data through the whole B-scan matrix, sub-matrices having localized information are utilized. For this purpose, a sliding window of a predetermined number of A-scans is swept through full B-scan to obtain submatrices as shown in Fig. 2. Each submatrix corresponds to $M_f \times L$ *sub*-B-scan denoted here as

$$\mathbf{B}_i^{sub} = \mathbf{B}_i^{sub}\left(\mathbf{R}_i^{L+i-1}, \omega\right) = \begin{pmatrix} A(\vec{r}_i, \omega_1) & \cdots & A\left(\vec{r}_{L+i-1}, \omega_1\right) \\ \vdots & \ddots & \vdots \\ A(\vec{r}_i, \omega_{M_f}) & \cdots & A\left(\vec{r}_{L+i-1}, \omega_{M_f}\right) \end{pmatrix} \tag{2}$$

where $i = 1, \ldots, N-L+1$, $L \leq N-i+1$ is the number of A-scans considered in a single sub-B-scan and M_f the number of frequency samples considered in the bandwidth. Note that there are a total of $N-L+1$ sub-B-scans. Applying SVD to $\mathbf{B}_i^{sub}$ yields $\mathbf{B}_i^{sub} = \mathbf{U}_i^{sub}\mathbf{\Lambda}_i^{sub}(\mathbf{V}_i^{sub})^\dagger$ where $\mathbf{U}_i^{sub}$ is the unitary $M_f \times M_f$ matrix of left singular vectors, $\mathbf{V}_i^{sub}$ is the unitary $L \times L$ matrix of right singular vectors and

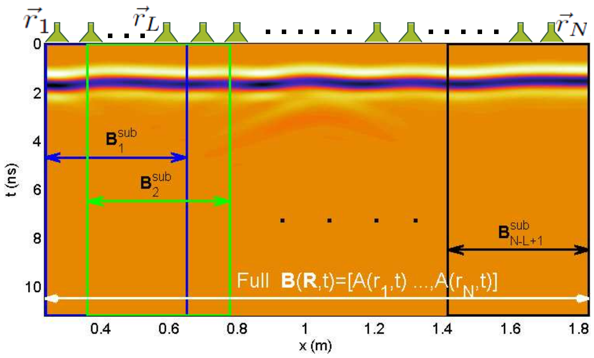

Figure 2. Sliding windows and corresponding sub-matrices (sub-radargrams) for the full B-scan of GPR survey obtained for the shallowly buried dielectric target under the rough surface of Fig. 1. Each sub-radargram is associated with a specific *synthetic* aperture determined by the recorded A-scan locations.

$\mathbf{\Lambda}_i^{sub}$ is the $M_f \times L$ matrix of singular values and $\dagger$ represents the conjugate transpose operator. Here, $\mathbf{B}_i^{sub}$ maps the local spatial information to the received frequency data via $\mathbf{B}_i^{sub}\mathbf{v}_{i,n}^{sub} = \lambda_{i,n}^{sub}\mathbf{u}_{i,n}^{sub}$ where $\lambda_{i,n}^{sub}$ is the nth singular value, $\mathbf{v}_{i,n}^{sub}$ is the nth $L \times 1$ *right* singular vector that represents the spatial (position) content of the received signals and $\mathbf{u}_{i,n}^{sub}$ is the nth $M_f \times 1$ *left* singular vector containing frequency information [15]. The left singular vectors, $\mathbf{u}_{i,n}^{sub}$ for $n = 1, \ldots, M_f$ are orthonormal and span the frequency space and they are the eigenvectors of the time-reversal operator (TRO) matrix $\mathbf{B}_i^{sub}(\mathbf{B}_i^{sub})^\dagger$. Similarly, the right singular vectors ($\mathbf{v}_{i,n}^{sub}$ for $n = 1, \ldots, L$) are also orthonormal and span the GPR location space. Assuming $M_f \geq L$ and utilizing the singular vectors, $\mathbf{B}_i^{sub}$ can be rewritten in the following form:

$$\mathbf{B}_i^{sub} = \sum_{n=1}^{L} \lambda_{i,n}^{sub}\mathbf{u}_{i,n}^{sub}\left(\mathbf{v}_{i,n}^{sub}\right)^* \tag{3}$$

Using the left singular vectors of each sub-B-scan, time-domain singular vectors can be constructed through inverse Fourier transform via $u_{i,n}^{sub}(t) = \mathcal{F}^{-1}\{\mathbf{u}_{i,n}^{sub}\}$. Depending on the scenario, each time-domain signal might correspond to different signatures of the scattering mechanisms in the GPR scenario. For illustration, several dominant time-domain singular vectors of the leftmost sub-B-scan ($u_{1,n}^{sub}(t)$ for $n = 1, \ldots, 3$) are compared with those of the full B-scan in Fig. 3. In this example, the full B-scan utilizes $N = 112$ A-scans whereas the sub-B-scan has only $L = 5$ A-scans. Since surface scattering is dominant for both cases, the first singular vectors correspond to the surface reflection. However, the remaining singular vectors show big differences: Those of the full B-scan mainly lie between 1–4 ns and correspond to an *effective* response from all $N = 112$ A-scans whereas those of the sub-B-scan are around 6–9 ns and correspond to localized target response at the particular GPR antenna distance. This shows the advantage of using sub-radargrams over the full B-scan as it can extract more localized information. The locality of information also applies for the first singular vectors. Under a rough surface profile, the first singular vector of the full B-scan provides a surface response similar to the ensemble average subtraction [1] which is effective only if the ground is uniform. But with the use of sub-B-scan, relatively local surface roughness is included with different time delays and amplitudes allowing better surface clutter reduction. It may be argued that for localized scatterers under uniform surface conditions, the full B-scan can give the same first singular vector (see Fig. 3), hence removes the surface scattering as effectively as sub-B-scan matrices. While this statement is absolutely valid, it should be kept in mind that for elongated scatterers under uniform surface, full B-scan cannot provide the same localized information as sub-B-scans. This constitutes yet another advantage of sub-B-scans over full B-scan.

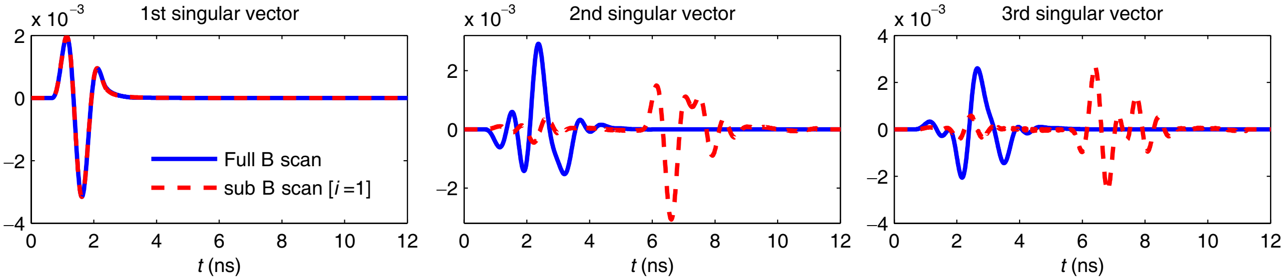

Figure 3. Time-domain singular vectors of the 1st sub-B-scan ($u_{1,n}^{sub}(t)$) are compared with those of the full B-scan for a dielectric target under a uniform surface profile.

Once the time-domain singular vectors of sub-B-scans are obtained, they can be combined to generate *synthetic* singular vector distributions given as follows:

$$\mathbf{C}_n\left(\mathbf{R}_1^{N-L+1}, t\right) = \left[u_{1,n}^{sub}(t), \ \ldots, \ u_{N-L+1,n}^{sub}(t)\right] \tag{4}$$

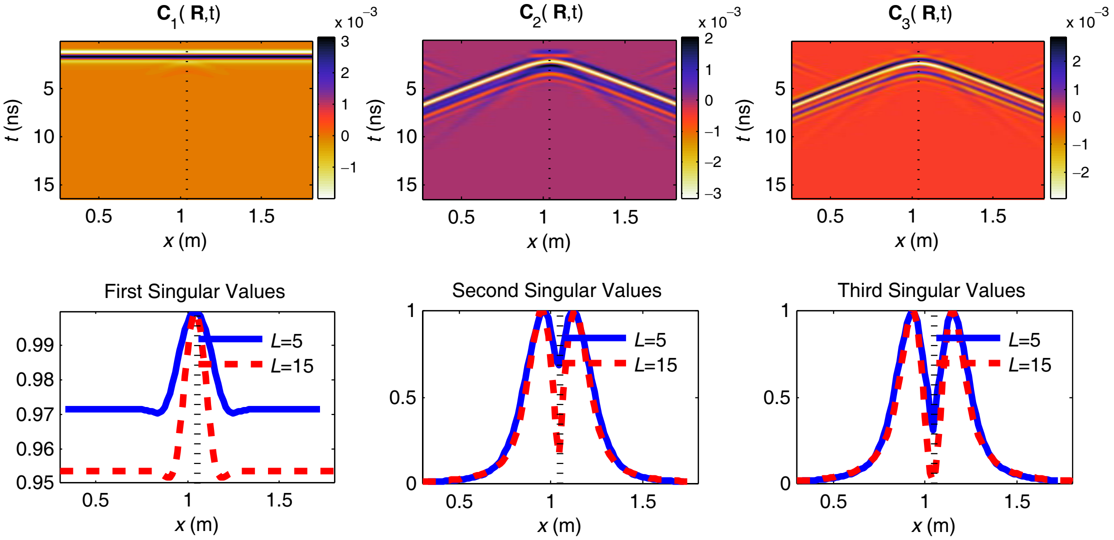

Figure 4. The first three dominant singular vector distributions ($\mathbf{C}_n(\mathbf{R}_1^{N-L+1}, t)$ for $n = 1,\ 2,\ 3$) for $L = 5$ and corresponding singular values (bottom) for a dielectric target under a uniform surface profile when $L = 5$ and $L = 15$. The vertical dashed lines represent the lateral target location.

Each of these distributions provides a global snapshot of distinct mechanisms of the scattering scenario as illustrated in Fig. 4 for the single dielectric target case of Fig. 3. From these figures, it is observed that, the first singular vector distribution is mostly dominated by the surface scattering. Thus, it can be later used to eliminate the surface clutter. The remaining distributions mostly correspond to the embedded target and exhibit somewhat close to the so-called *hyperbola* curve which is typical for isolated scatterers (Here, we have limited our study to pulse shaped radar waveforms and similar study can be performed for other waveforms as well). The peak of the hyperbola represents the lateral position of the target. In certain circumstances, the corresponding singular value distributions can also be used for change detection as they tend to peak or dip above the isolated targets [21]. The singular values and vectors can be combined together to obtain the following weighted singular vector distribution:

$$\mathbf{D}_n\left(\mathbf{R}_1^{N-L+1}, t\right) = \left[\lambda_{1,n}^{sub}\, u_{1,n}^{sub}(t),\ \ldots,\ \lambda_{N-L+1,n}^{sub}\, u_{N-L+1,n}^{sub}(t)\right] \tag{5}$$

This distribution can then be subtracted from the full B-scan to eliminate the surface clutter and thereby enhancing the target signatures where possible. The resulting matrices (distributions) can be denoted as *synthetic* residual B-scans and are represented by

$$\mathbf{S}_P\left(\mathbf{R}_1^{N-L+1}, t\right) = \mathbf{B}\left(\mathbf{R}_1^{N-L+1}, t\right) - \sum_{n=1}^{P} \mathbf{D}_n\left(\mathbf{R}_1^{N-L+1}, t\right) \tag{6}$$

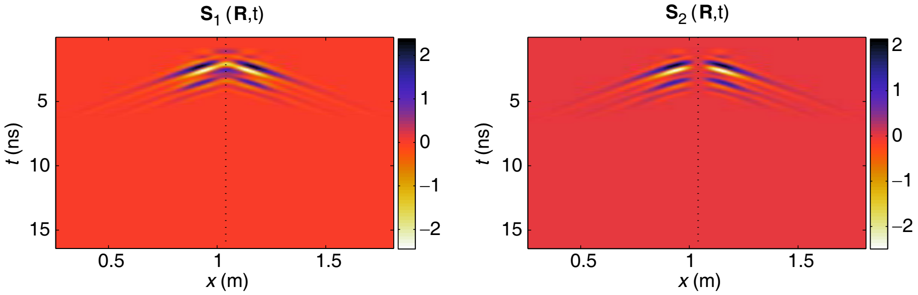

Figure 5. The first two residual distributions, i.e., synthetic B-scans ($\mathbf{S}_i(\mathbf{R}_1^{N-L+1}, t)$ for $i = 1,\ 2$) once the dominant singular vectors are subtracted from the full B-scan for uniform surface case.

where P is the number of individual weighted singular vector distributions. Fig. 5 shows two such synthetic B-scans obtained for the dielectric target under uniform surface profile for $P = 1$ and $P = 2$. Once compared with the full B-scan of Fig. 1, it is observed that the surface scattering from the full B-scan is eliminated and the target response (hyperbola) from the embedded dielectric scatterer is distinguishable. For this particular case, $\mathbf{S}_1$ is already enough for detecting the hyperbola curve.

Another point to note is the criteria to choose the radargram subsets which is highly scenario dependent. The number of total B-scans, the interval between each B-scan, central wavelength of operation, scatterer size and other factors affect the choice of subsets. As a rule of thumb, smaller subsets provide more localized information than the larger subsets. But if the subset is very small (e.g., $L = 1$), then singular vectors can not be necessarily utilized as described in the method. To our experience, depending on the scenario, subsets should be chosen encompassing a range of 1 to 2 wavelengths of interest. In some of the figures throughout the paper, we have provided the singular vector distributions for both $L = 5$ and $L = 15$ for comparison.

3. FURTHER SIMULATION RESULTS AND DISCUSSIONS

Here, the algorithm is applied to several scenarios to assess its performance under different conditions.

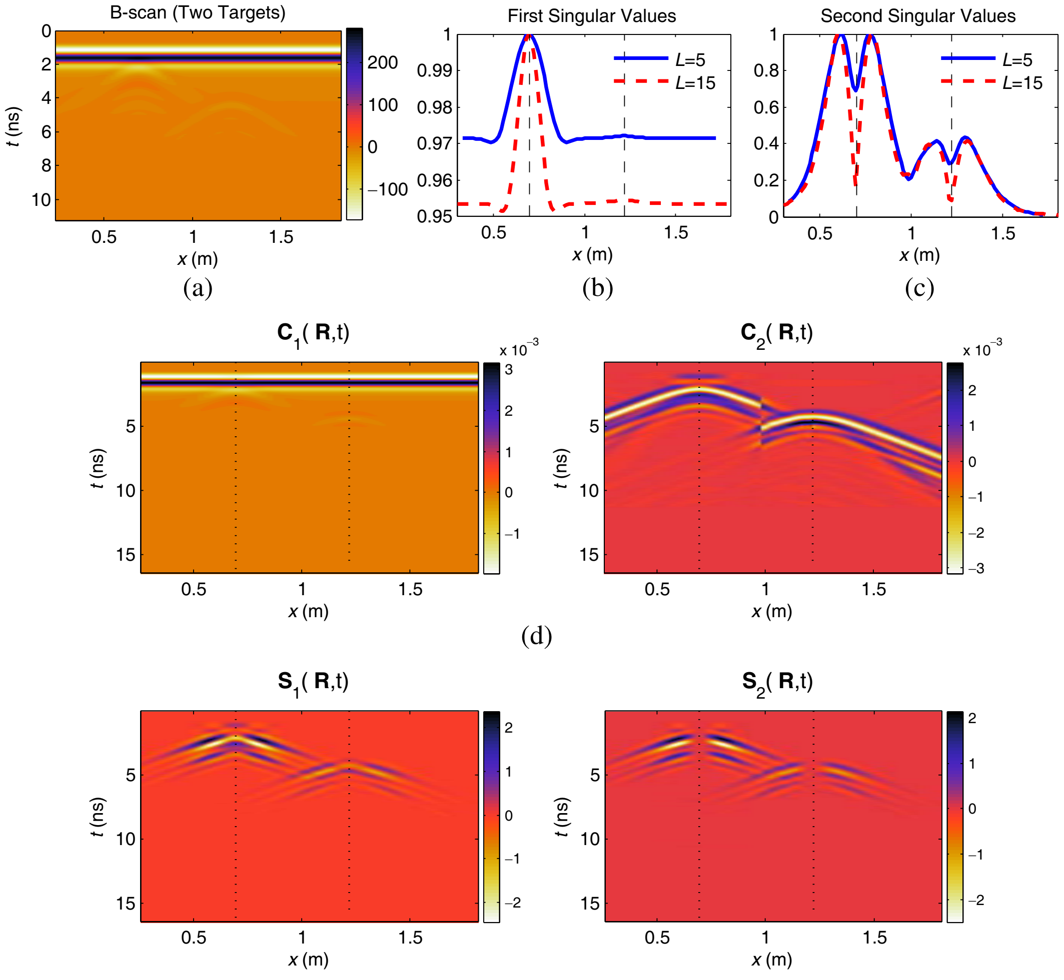

(a) (b) (c)

(d)

(e)

Figure 6. (a) Full B-scan of the scenario with two dielectric scatterers. Corresponding first and second singular value distribution along the survey path (c) singular vector distributions are shown in the following rows (d). Finally, the residual distributions are shown in (e).

3.1. Multiple Targets Case

We start by testing the algorithm for two dielectric targets embedded under a uniform surface profile at $x = 0.7\,\mathrm{m}$ and $x = 1.22\,\mathrm{m}$ and having relative dielectric permittivities of $\epsilon_r = 3$ and $\epsilon_r = 4.5$, respectively. While the first one (on left) is at a depth of 5 cm from the surface, the second one on the right is at 15 cm. Since the dielectric permittivity of the right one is larger, its dielectric contrast with the background is smaller compared to the left one. Hence, it poses a more difficult detection problem than the left one. As shown in Fig. 6, the full B-scan is again dominated by the surface scattering. The signature from the deeper target is almost invisible at this stage. Once the aforementioned procedure is applied, several distinct patterns become available for further analysis. For example, it is observed that the first dominant singular value distribution along the survey path is relatively constant except for a small fluctuation over the shallower target. Albeit small, this can be considered as peaks over the target locations. On the other hand, the second dominant singular value distribution exhibits an increase as the GPR unit gets closer to the scatterers along with a null just over the scatterers. The null value seems to be sharper when a larger L value is utilized. Thus, in some cases merely monitoring the changes in the singular value distributions along the survey path can provide partial target localization information. As for the synthetic singular vector distributions, the first one $\mathbf{C}_1(\mathbf{R}_1^{N-L+1}, t)$ in this case is also dominated by the surface scattering whereas the remaining ones exhibit two hyperbolic curves each corresponding to different targets. Tracking the maxima of the hyperbola curves at this stage allows lateral target localization. Also, relative differences between the maxima provide relative depth information about the scatterers. Once the singular values and vectors are used together and subtracted from the full B-scan, the resulting residual synthetic B-scans ($\mathbf{S}_i(\mathbf{R}_1^{N-L+1}, t)$) again reveal the hyperbola curves corresponding to the two targets in the domain without any ground reflection. Note also that if the full B-scan was used in this case, the obtained time-domain signals would be linear combination

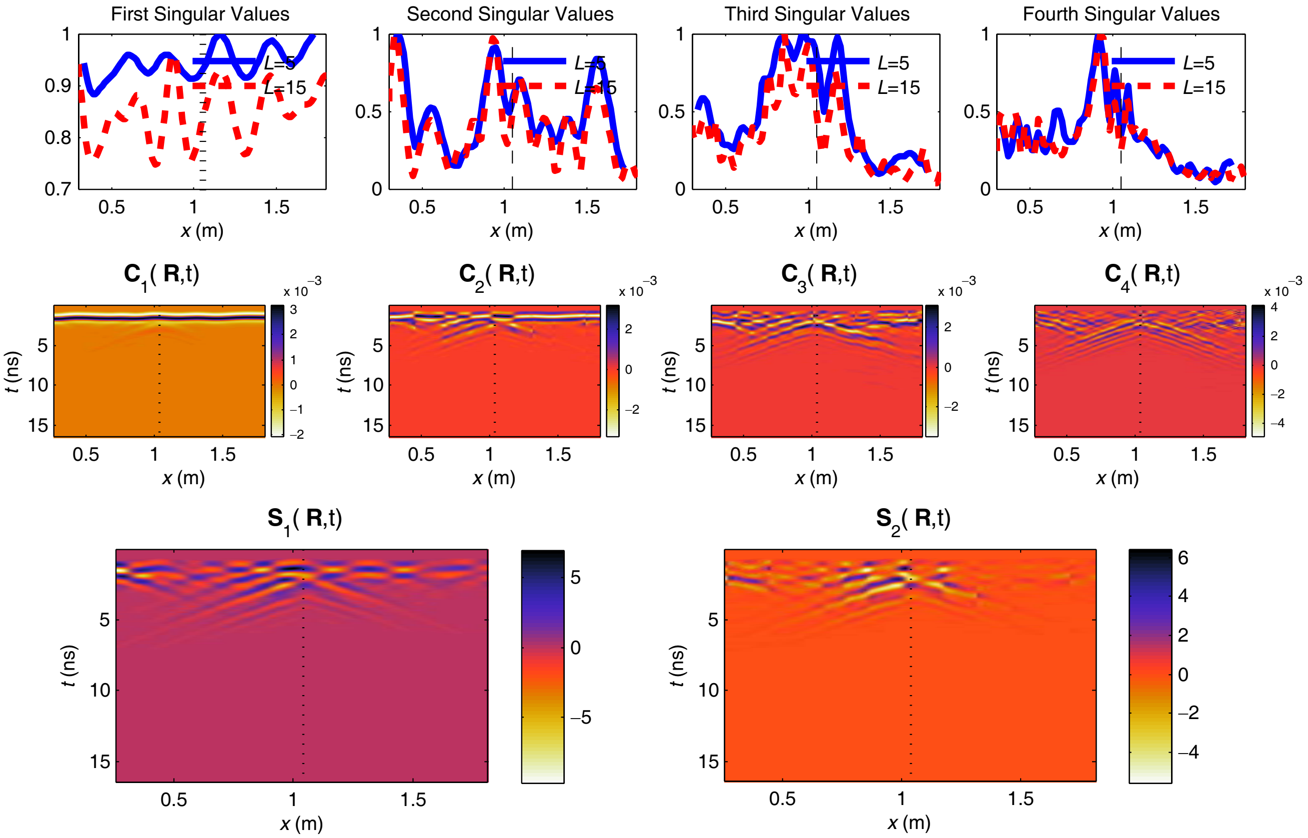

Figure 7. The first four singular value and synthetic singular vector distributions for a *dielectric* target under random surface are shown along with the first two of the resulting residual distributions.

of the signatures from both targets as they are not well resolved. Using localized information through sliding windows is helpful to distinguish both target signatures in this case.

3.2. Single Dielectric Target under Rough Surface Profile

In many practical scenarios, the ground surface can exhibit roughness. In this section, we apply the algorithm for a single dielectric target of $\epsilon_r = 3$ under randomly fluctuating surface profile as shown in Fig. 1. The surface has a standard deviation of 5 cm and correlation length of 30 cm. The corresponding full B-scan for this case is already shown in Fig. 2. Corresponding singular value distributions along the lateral position are shown in Fig. 7. The first two singular values are dominated by the surface scattering, thus do not exhibit a certain profile. However, similar to the uniform surface case, the 3rd and 4th singular value distributions demonstrate increasing patterns as the GPR unit gets closer to the target and partial null focusing above the scatter location. Once the associated synthetic singular vector distributions shown in the same figure are analyzed, it is observed that when the surface is random, the first two singular vector distributions are mainly dominated by surface reflections. Although some traces of hyperbola can be distinguished in the second distribution, no clear hyperbola exists in the first distributions. As for the third distribution, the hyperbola is clearer but there is also contributions from the surface scattering. A similar pattern exists for the fourth distribution with clearer hyperbola curve. Once the residual distributions are obtained by subtracting the singular vectors weighted by associated singular values from the full B-scan, the response from the dielectric target becomes more visible. This is somewhat expected as the surface scattering mainly dominates the higher singular values/vectors and as they are taken out of the full B-scan, remaining contributions reveal the dielectric target response. Note also that once the larger contributions of the surface scattering are less pronounced (e.g., in $\mathbf{C}_3$ or $\mathbf{C}_4$), then time gating can be applied to further reveal the hyperbola curves observed in synthetic

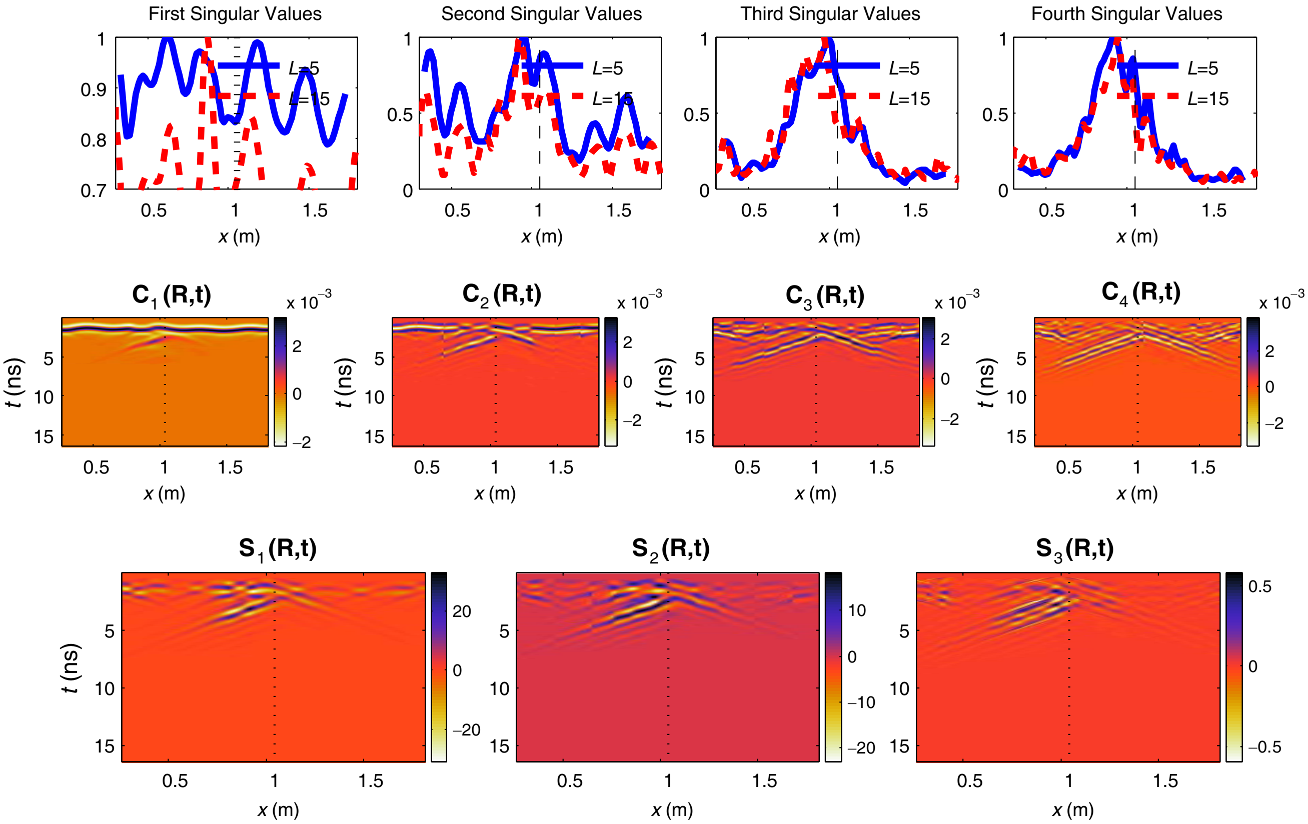

Figure 8. The first four singular value and synthetic singular vector distributions for a *metallic* target under random surface are shown along with the first two of the resulting residual distributions.

singular vector distributions (not applicable to residual distributions if their complete subtractions are considered).

3.3. Single Metallic Target under Rough Surface Profile

It is observed that with the rough surface and shallowly buried dielectric target, the dominant singular values and vectors are mainly due to the surface reflection. Thus, the performance of the proposed method degrades with the rough surface case. However, when the target contrast is higher (e.g., in the case of metallic unexploded ordnances) and the surface is rough, the algorithm can still be helpful in distinguishing different scattering mechanism of a given scenario. For this purpose, we apply the method to an embedded metallic scatterer under a rougher surface profile with variance of 10 cm. The resulting singular value and vector distributions are shown in Fig. 8. Similar to the previous cases, the first two singular values are dominated by the surface scattering. However, an increasing pattern when the GPR unit is closer to the scatterer is clearly visible for both third and fourth singular value distributions. As for the synthetic singular vector distributions, the contributions from the surface scattering are clearly visible in all four distributions with $\mathbf{C}_4(\mathbf{R}_1^{N-L+1}, t)$ being the least affected. Hyperbola curves are clearly visible for the second, third and fourth cases revealing the lateral location of the isolated scatterer. Similarly, resulting residual distributions clearly show the response of the metallic scatterer.

4. CONCLUSIONS AND FUTURE WORKS

We introduced a GPR signal processing method based on the sliding-window space-frequency matrices. A full B-scan obtained during a GPR survey is decomposed into submatrices using the sliding windows. Each submatrix is later processed similar to the space-frequency TR imaging concept of [15]. The processing provides localized scattering center signatures in a combined fashion cast in terms of so-called synthetic singular vector distributions. Once combined with the associated singular values and subtracted from the full B-scan, the method can achieve GPR signal enhancement by mainly reducing clutter from the surface reflection. The method also has the potential for utilization with other methods such as time gating for improved performance. Although subsurface application is shown here, the method can also be applied to other applications such as through-wall imaging (TWI). Using the same method, the wall reflections in a TWI scenario can be successfully removed. This also constitutes one of our avenues for future work. Similarly, the same method can be applied to the detection of reservoir beds by classifying the scattering centers appropriately. Extension to array configurations instead of single transceivers can also be considered.

REFERENCES

1. Daniels, D. J., *Ground Penetrating Radar*, 2nd edition, IEE, London, UK, 2004.
2. Dogaru, T. and L. Carin, "Time-domain sensing of targets buried under a rough air-ground interface," *IEEE Trans. Antennas Propagat.*, Vol. 46, No. 3, 360–372, March 1998.
3. Brunzell, H., "Detection of shallowly buried objects using impulse radar," *IEEE Trans. Geosci. Remote Sensing*, Vol. 37, No. 2, 875–886, March 1999.
4. Potin, D., E. Duflos, and P. Vanheeghe, "Landmines ground-penetrating radar signal enhancement by digital filtering," *IEEE Trans. Geosci. Remote Sens.*, Vol. 44, No. 9, 2393–2406, September 2006.
5. Van der Merwe, A. and I. J. Gupta, "A novel signal processing technique for clutter reduction in GPR measurements of small, shallow land mines," *IEEE Trans. Geosci. Remote Sensing*, Vol. 38, No. 6, 2627–2637, November 2000.
6. Xu, X., E. L. Miller, C. M. Rappaport, and G. D. Sower, "Statistical method to detect subsurface objects using array ground-penetrating radar data," *IEEE Trans. Geosci. Remote Sensing*, Vol. 40, No. 4, 963–976, April 2002.
7. Gunatilaka, A. H. and B. A. Baertlein, "Subspace decomposition technique to improve gpr imaging of antipersonnel mines," *Proc. SPIE 4038, Detection and Remediation Technologies for Mines and Minelike Targets*, Vol. V, 1008, August 2000.

8. Abujarad, F., A. Jostingmeier, and A. Omar, "Clutter removal for landmine using different signal processing techniques," *Proc. of the Tenth IEEE Int. Conf. on Ground Penetrating Radar GPR 2004*, 697–700, June 2004.
9. Abujarad, F., G. Nadim, and A. Omar, "Clutter reduction and detection of landmine objects in ground penetrating radar data using singular value decomposition (SVD)," *2005 Proc. of the 3rd Int. Workshop on Advanced Ground Penetrating Radar IWAGPR*, 37–42, May 2–3, 2005.
10. Solimene, R. and A. D'Alterio, "Entropy-based clutter rejection for intrawall diagnostics," *International Journal of Geophysics*, Vol. 2012, No. Article ID 418084, 7 pages, 2012.
11. Brooks, J. W., L. M. V. Kempen, and H. Sahli, "Primary study in adaptive clutter reduction and buried minelike target enhancement from GPR data," *Proc. SPIE*, Vol. 4038, 1183–1192, 2000.
12. Vicen-Bueno, R., R. Carrasco-Alvarez, M. Rosa-Zurera, and J. Nieto-Borge, "Sea clutter reduction and target enhancement by neural networks in a marine radar system," *Sensors*, Vol. 9, No. 3, 1913–1936, 2009.
13. Roy, S. and J. Maheux, "Baseline processing pipeline for fast automatic target detection and recognition in airborne 3D ladar imagery," *Proc. SPIE*, Vol. 8049, 80490S, 2011.
14. Vicen-Bueno, R., M. Rosa-Zurera, M. Jarabo-Amores, and R. Gil-Pita, "Automatic target detection in simulated ground clutter (weibull distributed) by multilayer perceptrons in a low-resolution coherent radar," *IET Radar, Sonar & Navigation*, Vol. 4, No. 2, 315–328, 2010.
15. Yavuz, M. E. and F. L. Teixeira, "Space-frequency ultrawideband time-reversal imaging," *IEEE Trans. Geosci. Remote Sensing*, Vol. 46, No. 4, 1115–1124, 2008.
16. Fink, M., D. Cassereau, A. Derode, C. Prada, P. Roux, M. Tanter, J. Thomas, and F. Wu, "Timereversed acoustics," *Rep. Prog. Phys.*, Vol. 63, 1933–1995, 2000.
17. Fouda, A. E., F. L. Teixeira, and M. E. Yavuz, "Time-reversal techniques for MISO and MIMO wireless communication systems," *Radio Sci.*, Vol. 47, RS0P02, 2012.
18. Yavuz, M. E. and F. L. Teixeira, "Ultrawideband microwave sensing and imaging using time-reversal techniques: A review," *Remote Sens.*, Vol. 1, No. 3, 466–495, 2009.
19. Foroozan, F. and A. Asif, "Time-reversal ground-penetrating radar: Range estimation with Cramer-Rao lower bound," *IEEE Trans. Geosci. Remote Sens.*, Vol. 48, No. 10, 3698–3708, October 2010.
20. Zhu, X., Z. Zhao, W. Yang, Y. Zhang, Z. Nie, and Q. H. Liu, "Iterative time-reversal mirror method for imaging the buried object beneath rough ground surface," *Progress In Electromagnetics Research*, Vol. 117, 19–33, 2011.
21. Potin, D., P. Vanheeghe, E. Duflos, and M. Davy, "An abrupt change detection algorithm for buried landmines localization," *IEEE Trans. Geosci. Remote Sens.*, Vol. 44, No. 2, 260–272, Febuary 2006.
22. Moss, C. D., F. L. Teixeira, Y. E. Yang, and J. A. Kong, "Finite-difference time-domain simulation of scattering from objects in continuous random media," *IEEE Trans. Geosci. Remote Sensing*, Vol. 40, 178–186, 2002.
23. Yavuz, M. E., A. E. Fouda, and F. L. Teixeira, "Target classification through time-reversal operator analysis using ultrawideband electromagnetic waves," *Proc. of the 5th European Conf. on Antennas and Propagation (EUCAP)*, 14–18, April 2011.